Least Squares Restoration of Multichannel Images

Nikolas P. Galatsanos, *Member, IEEE,* Aggelos K. Katsaggelos, *Member, IEEE,* Roland T. Chin, *Member, IEEE,* and Allen D. Hillery, *Member, IEEE*

Abstract—**In this paper we consider the problem of multichannel restoration using both within- and between-channel deterministic information. A multichannel image is a set of image planes that exhibit cross-plane similarity. Existing optimal restoration filters for single-plane images will yield suboptimal results when applied to multichannel images, since between-channel information is not utilized. Multichannel least squares restoration filters are developed using two approaches, a set theoretic and a constrained optimization. A geometric interpretation of the estimates of both filters is given. Color images, that is, three-channel imagery with red, green, and blue components, are considered. Constraints that capture the within- and between-channel properties of color images are developed. Issues associated with the computation of the two estimates are addressed. A spatially adaptive, multichannel least squares filter that utilizes local within- and between-channel image properties is proposed. Finally, experiments using color images are shown.**

I. Introduction

THE use of image data from multiple frequency bands, multiple time frames, or multiple sensors can be of tremendous value in a number of applications, such as multispectral satellite remote sensing, multisensor robot guidance, and multimedium medical diagnosis. Of special interest are color images, due to their wide range of applications. Color can be regarded as a set of three images in their primary color components. In this paper, we shall use the general term of multichannel images to indicate that we are dealing with multiple image channels (planes) obtained by an imaging system that measures the same scene using more than one type of sensor.

In most applications, the multichannel images are distorted, due to, for example, motion, out-of-focus blur, channel crosstalk, registration error, quantization error, and device noise. Therefore, restoration of multichannel images is required before further possible human or machine analysis. More specifically, the following degradation model is considered:

$$\boldsymbol{g} = \boldsymbol{H}\boldsymbol{f} + \boldsymbol{n} \tag{1.1}$$

Manuscript received February 15, 1989; revised September 10, 1990. This work was supported by NSF ECS-8352356, NASA NAG 5-580, U.W.WARF Foundation and NSF MIP 8614217.

N. P. Galatsanos is with the Department of Electrical and Computer Engineering, Illinois Institute of Technology, Chicago, IL 60616.

A. K. Katsaggelos is with the McCormick School of Engineering and Applied Science, Department of Electrical Engineering and Computer Science, Northwestern University, Evanston, IL 60208.

R. T. Chin and A. D. Hillery are with the Department of Electrical and Computer Engineering, University of Wisconsin, Madison, WI 53706.

IEEE Log Number 9101885.

where $\boldsymbol{g}$, $\boldsymbol{f}$, and $\boldsymbol{n}$ represent the observed image, the original image, and the noise, respectively. For N channels $M \times M$ pixels each, they are given by

$$\boldsymbol{g} = \begin{bmatrix} g_1 \\ g_2 \\ \vdots \\ g_i \\ \vdots \\ g_N \end{bmatrix} \quad \boldsymbol{f} = \begin{bmatrix} f_1 \\ f_2 \\ \vdots \\ f_i \\ \vdots \\ f_N \end{bmatrix} \quad \boldsymbol{n} = \begin{bmatrix} n_1 \\ n_2 \\ \vdots \\ n_i \\ \vdots \\ n_N \end{bmatrix} \tag{1.2}$$

where each of the M^2 vectors g_i, f_i, n_i results from the lexicographic ordering of the two-dimensional signals in each channel [2]. The $NM^2 \times M^2N$ multichannel degradation matrix $\boldsymbol{H}$ is equal to

$$\boldsymbol{H} = \begin{bmatrix} H_{11} & H_{12} & \cdots & H_{1N} \\ H_{21} & H_{22} & \cdots & H_{2N} \\ \vdots & \vdots & \cdots & \vdots \\ H_{N1} & H_{N2} & \cdots & H_{NN} \end{bmatrix}. \tag{1.3}$$

Submatrices H_{ii} and H_{ij}, for $i \neq j$ are of dimension $M^2 \times M^2$ and represent the within-channel and the cross-channel degradation, respectively. Throughout this paper we assume only within-channel shift-invariant imaging systems. This assumption yields H_{ij} block Toeplitz matrices. However, $\boldsymbol{H}$ is not Toeplitz, since no shift invariance across channels is assumed, that is, $H_{ij} \neq H_{i+k,j+k}$.

Although there is a large amount of work in the literature on digital restoration of single-channel images [2], [33], there has been little investigation of multichannel restoration. Processing of multichannel images is substantially different from that of single-channel images. The extension of existing single-channel images restoration techniques to multichannel restoration is a nontrivial and difficult task. Filters that are optimal for single-channel images may be suboptimal when applied individually to the separate channels of a multichannel image. For example, in the detection of a signal, the signature of the signal that appears only weakly in individual image channels, and may therefore go undetected using conventional single-channel processing, may appear strong in a multichannel processing scheme because of its presence in all channels, and therefore may be easily detected.

1053-587X/91/1000-2222$01.00 © 1991 IEEE

The first reported research on multichannel restoration is by Hunt and Kubler [12]. They derived a minimum MSE multichannel restoration filter based on the assumption that the multichannel correlation, describing the cross-channel and spatial (within-channel) relationship, is separable. This enables the decorrelation of the channels based on the Karhunen–Loeve transformation. Therefore, subsequent filtering of individual channels can be done by conventional single-channel image restoration algorithms. However, the separability assumption is too limiting, and this method cannot handle the case when cross-channel degradation is present, that is, $H_{ij} \neq 0$ for $i \neq j$.

A restoration filter for color images based on the idea of [12] is reported in [23]. Additional results on the restoration of color images are reported in [3], [16], and [28]. In [9], [15], and [18] an imaging model consisting of identical images in all channels blurred by different blurs was used to compute a least squares solution. This solution was computed without explicitly using any cross-channel information.

We believe there is much to be gained by incorporating the interdependency between the cross-channel and spatial correlations in multichannel restoration. Such minimum MSE filters have been developed, and their results are reported in [5]–[8]. These filters utilize the cross-channel correlations without using the separability assumption. Also, they can handle the case $H_{ij} \neq 0$ for $i \neq j$.

A significant amount of prior knowledge is required for the multichannel minimum MSE filter. Although the filter is optimally derived, its true success in restoring real-world images depends on accurate statistical knowledge of the signal and noise as random variables. To be more specific, the minimum MSE filter requires accurate estimation of the image and noise power spectra.

Another serious drawback of multichannel minimum MSE filtering is the fact that it is extremely sensitive to the estimate of the cross-channel spectra, see [5] and [27]. It was shown in [27] that traditional single-channel spectral estimation methods (e.g., periodogram estimates of windowed prototype images) fail in multichannel restoration because cross-channel spectra contain phase information.

Other criteria may be used for the development of optimal restoration filters. A number of them have been investigated by various researchers for single-channel restoration, including the minimization of the Laplacian for spatial smoothness and the minimization of entropy for global smoothness. The application of constrained least squares approaches to single-channel image restoration was first proposed in [11] and later investigated by other researchers. See, for example, [14], [17], [20], and [32].

In this paper the least squares approach is used to solve the multichannel restoration problem. Deterministic *a priori* information of between- and within-channel is used. This alleviates some of the problems associated with the minimum MSE filter. Two approaches, a set theoretic and a constrained optimization, were used to derive restoration filters. Both methods yield solutions of the same form. Geometric interpretations and properties of these solutions are examined. Regularization theory of ill-posed problems [30] is used to justify and explain our results.

The multichannel problem is formulated and discussed in detail in Section II. In Section III we consider the implementation of our multichannel restoration filters. A spatially adaptive least squares multichannel filter is proposed in Section IV. Experimental results using color images and a comparative study are presented in Section V and in Section VI we present our conclusions.

II. Multichannel Constrained Least Squares Restoration

A. Set Theoretic Approach

Let us first denote the degradation function associated with the ith channel by the $M^2 \times NM^2$ matrix

$$\overline{H}_i = [H_{i1}, H_{i2}, \cdots, H_{iN}] \tag{2.1}$$

where H_{ij} represents the cross-channel degradation between channels i and j and H_{ii} the within-channel spatial degradation. The linear space-invariant degradation model defined by (1.1) can then be rewritten as

$$g_i = \overline{H}_i \boldsymbol{f} + n_i \qquad i = 1, 2, \cdots, N. \tag{2.2}$$

In this section, a set theoretic approach [25], which has been applied to single-channel restoration [19], and to the restoration of an image when multiple distorted versions of it are available [18], is used to estimate a solution to (2.2). More specifically, *a priori* knowledge about $\boldsymbol{f}$ is assumed which restricts the solution to lie in a set, that is,

$$\boldsymbol{f} \in S_f \tag{2.3}$$

where S_f is an NM^2-dimensional space. Similarly, the noise n_i is assumed to belong to a set S_{n_i}. Since n_i must lie in a set, it follows that a given observation g_i combines with the set S_{n_i} to define a new set which must contain $\boldsymbol{f}$. Thus the observation g_i specifies a set S_{f/g_i} which must contain $\boldsymbol{f}$, i.e.,

$$\boldsymbol{f} \in S_{f/g_i} = [\boldsymbol{f} : (\overline{H}_i \boldsymbol{f} - g_i) \in S_{n_i}]. \tag{2.4}$$

Consider now the sets $S_f, S_{f/g_1}, \cdots, S_{f/g_N}$. Each set contains $\boldsymbol{f}$ and, therefore, $\boldsymbol{f}$ must lie in their intersection. Let $S_{\hat{f}}$ denote this intersection. Then

$$S_{\hat{f}} = S_f \cap S_{f/g_1} \cap \cdots \cap S_{f/g_N} \tag{2.5}$$

where $\cap$ denotes set intersection. According to (2.5), the restored image is not defined as a single vector but instead as a set. This set is the smallest set which must contain $\boldsymbol{f}$ and which can be calculated from the available information. We note here that the formulation of this set theoretic approach to restoration is quite straightforward and holds true for any kind of sets. However, the difficulty of the approach arises when the intersection of these sets defined in (2.5), is to be calculated. To make the problem more tractable, ellipsoids are used for the sets S_f and S_{n_i}.

The equation for an ellipsoid is given by

$$S_f = [\boldsymbol{f} : (\boldsymbol{f} - c_f)^t G_f^{-1} (\boldsymbol{f} - c_f) \leq 1] \tag{2.6}$$

where c_f is the center of the ellipsoid and G_f a positive matrix, whose eigenvalues and eigenvectors determine, respectively, the orientation and the lengths of the axis of S_f.

A usual form of the ellipsoids S_f and S_{n_i} is

$$\|\boldsymbol{Qf}\|^2 \leq E^2 \tag{2.7}$$

and

$$\|n_i\|^2 \leq \epsilon_i^2, \qquad i = 1, 2, \cdots, N \tag{2.8}$$

where $\|\cdot\|$ represents the Euclidean norm. Details about the role and the selection of the regularization operator $\boldsymbol{Q}$ are given in Section II-D. However, the intersection of ellipsoids is not necessarily an ellipsoid. Therefore, one approach to geometrically describe the intersection is to consider an ellipsoid which bounds the intersection [26]. Then we choose the center of this bounding ellipsoid to represent the restored image. For the ellipsoids of (2.7) and (2.8) it is shown in Appendix A that the center of the bounding ellipsoid is given by

$$\hat{\boldsymbol{f}} = \left[\sum_{i=1}^{N} p_i \frac{\overline{H}_i^t \overline{H}_i}{\epsilon_i^2} + p_{N+1} \frac{\boldsymbol{Q}^t \boldsymbol{Q}}{E^2} \right]^{-1} \cdot \left[\sum_{i=1}^{N} p_i \frac{\overline{H}_i^t}{\epsilon_i^2} g_i \right] \tag{2.9}$$

where $\Sigma_{i=1}^{N} p_i \leq 1$ and $p_i \leq 0$. For each choice of the values of p_i a different bounding ellipsoid is defined whose center corresponds to a different estimate of the original image. If all the p_i's are chosen to be equal then (2.9) yields

$$\left[\sum_{i=1}^{N} \lambda_i \overline{H}_i^t \overline{H}_i + \boldsymbol{Q}^t \boldsymbol{Q} \right] \hat{\boldsymbol{f}} = \sum_{i=1}^{N} \lambda_i \overline{H}_i^t g_i \tag{2.10}$$

where $\lambda_i = (E/\epsilon_i)^2$. Equation (2.10) can also be derived [18] by considering Miller's regularization approach [22], which was applied to the restoration of single channel images in [14]. As is clear from the above formulation, an estimate of the parameters E^2 and ϵ_i^2 must be obtained before this method can be used. Estimating ϵ_i the power of the additive white noise from the observed images, is a well-researched problem and a number of approaches have been proposed [2], [21]. We will discuss ways for obtaining an estimate for E later in this paper.

B. Constrained Optimization Approach

If E is not available *a priori*, or no satisfactory estimate can be obtained, a constrained optimization approach to multichannel restoration is followed next. Such an approach also results in (2.10) although the λ's are now unknown. According to this approach, an $\hat{\boldsymbol{f}}$ is sought which

$$\text{Minimizes } \|\boldsymbol{Qf}\|^2 \tag{2.11a}$$

$$\text{subject } \|\overline{H}_i \boldsymbol{f} - g_i\|^2 = \|n_i\|^2 = \epsilon_i^2 \quad \text{for } i = 1, 2, \cdots, N. \tag{2.11b}$$

Using the method of Lagrange multipliers, the solution $\hat{\boldsymbol{f}}$ is obtained by minimizing

$$\Phi(\boldsymbol{f}, \lambda) = \sum_{i=1}^{N} \lambda_i (\|\overline{H}_i \boldsymbol{f} - g_i\|^2 - \|n_i\|^2) + \|\boldsymbol{Qf}\|^2 \tag{2.12}$$

where $\lambda = (\lambda_1, \lambda_2, \cdots, \lambda_N)$ is the Lagrange multiplier vector. The Lagrangian method is based on the possibility of solving a system of equations which constitute necessary conditions of optimality. For the problem described by (2.11a) and (2.11b) these conditions are

$$\nabla_f \Phi(\boldsymbol{f}, \lambda) = 0 \tag{2.13a}$$

$$\nabla_\lambda \Phi(\boldsymbol{f}, \lambda) = 0 \tag{2.13b}$$

where ∇_z denotes the gradient of a function with respect to vector z. The Lagrange multiplier method consists of solving a sequence of unconstrained problems of (2.13a). The solution $\boldsymbol{f}(\lambda)$ is examined if it satisfies (2.13b) and λ is adjusted appropriately. The condition in (2.13b) results in (2.10) while condition (2.13b) results in (2.11b). The above optimization approach with the use of weighted norms was also followed in [15] when multiple distorted versions of the same image are available.

Using the multichannel notation, (2.10) yields

$$[\Lambda \boldsymbol{H}^t \boldsymbol{H} + \boldsymbol{Q}^t \boldsymbol{Q}] \hat{\boldsymbol{f}} = \Lambda \boldsymbol{H}^t \boldsymbol{g} \tag{2.14}$$

where $\boldsymbol{H}$ is the multichannel degradation as defined in (1.3) and Λ is defined as

$$\Lambda = \begin{bmatrix} \lambda_1[\boldsymbol{I}] & 0 & \cdots & 0 \\ 0 & \lambda_2[\boldsymbol{I}] & \cdots & 0 \\ \vdots & \vdots & \cdots & \vdots \\ 0 & 0 & \cdots & \lambda_N[\boldsymbol{I}] \end{bmatrix}$$

where the identity matrices $[\boldsymbol{I}]$ are of size $M^2 \times M^2$. Finally, solving for $\hat{\boldsymbol{f}}$ in (2.14) yields

$$\hat{\boldsymbol{f}} = [\boldsymbol{H}^t \boldsymbol{H} + \Lambda^{-1} \boldsymbol{Q}^t \boldsymbol{Q}]^{-1} \boldsymbol{H}^t \boldsymbol{g} \tag{2.15}$$

which is the solution of the constrained least squares restoration with respect to chosen values of the parameters in $\boldsymbol{Q}$.

The solution $\hat{\boldsymbol{f}}(\lambda_1, \lambda_2, \cdots, \lambda_N)$ in (2.15) must satisfy the constraint (2.11b), which can be written as

$$Z_i(\lambda_1, \lambda_2, \cdots, \lambda_N) = (\|\overline{H}_i \hat{\boldsymbol{f}} - g_i\|^2 - \|n_i\|^2) \quad \text{for } i = 1, 2, \cdots, N. \tag{2.16}$$

Finding the roots of the functions $Z_i(\lambda_1, \lambda_2, \cdots, \lambda_N)$ simultaneously yields the desired λ_i. The functions $Z_i(\lambda_1, \lambda_2, \cdots, \lambda_N)$ are nonlinear, therefore Newton's method is used to find the λ_i numerically. The details of the computation of the Jacobian of this system are given in Appendix B. The main drawback of this approach is the high computational cost of the Newton iterations.

If we assume there is only spatial blur and no cross-channel constraints, that is, both $\boldsymbol{H}$ and $\boldsymbol{Q}$ are block diagonal matrices (a block diagonal matrix $\boldsymbol{H}$ of dimension $NM^2 \times M^2N$ is a matrix with submatrices H_{ij} of dimension $M^2 \times M^2$, where $H_{ij} = 0$ for $i \neq j$), then (2.10) degenerates into independent single-channel least squares filtering given by

$$\hat{f}_i = \left[H_{ii}^t H_{ii} + \frac{1}{\lambda_{ii}} Q_{ii}^t Q_{ii} \right]^{-1} H_{ii}^t g_i \quad \text{for } i = 1, 2, \cdots, N. \tag{2.17}$$

C. Geometric Interpretation

Let us now compare and geometrically characterize the solutions obtained by both approaches. These solutions are, respectively, denoted by f_b and f_{CLS}. They are shown in Fig. 1 for a two-dimensional example, with $N = 2$. With the constrained optimization approach, the prior knowledge defines only the ellipsoids S_{f/g_1} and S_{f/g_2}. Then the restored image f_{CLS} is the point of intersection of the two ellipsoids to which the center $f = 0$ of the ellipsoid S_f is closest.

With the set theoretic approach, the ellipsoid S_f is defined together with the ellipsoids S_{f/g_1} and S_{f/g_2}. The restored image f_b is the center of the bounding ellipsoid which encloses the intersection of the three ellipsoids, denoted by S_b in Fig. 1. Provided that such an f_b belongs to S_b, f_b is clearly inside both ellipsoids S_{f/g_1} and S_{f/g_2}. As compared to f_{CSL}, f_b is closer to both centers, denoted, respectively, by f_i^+ and f_2^+, of the two ellipsoids. These centers represent the generalized inverse solutions of the individual image channels given by (A.9) in Appendix A. In the case of ill-conditioned degradation matrices $\bar{H}_i$, noise amplification results in noisy solutions f_1^+ and f_2^+.

By examining Fig. 1, it is clear that by reducing the value of E, the size of the ellipsoid S_f reduces, and the solution f_b moves closer to f_{CLS}. Small values of E result in small values of λ_i in (2.10). Since $1/\lambda_i$ are the regularization coefficients of (2.10) that tradeoff smoothness and data fidelity [30], we expect that a small E produces a smooth solution. In other words, the solution obtained by (2.10) is noisier than that obtained by (2.15) with E unknown, because the coefficients $1/\lambda_i$ are smaller in the former case. These properties of the solutions f_b and f_{CLS} have been verified experimentally in Section V.

D. Selecting the Regularization Operator $\boldsymbol{Q}$

It is well known that the solution of (1.1) represents an ill-posed problem, which means that matrix $\boldsymbol{H}$ is ill conditioned [2]. Thus the estimate $\hat{f}$ in (2.15) represents the regularized solution of the imaging equation (1.1). In that context operator $\|\boldsymbol{Qf}\|$ plays the role of a regularizing functional. The role of this $\boldsymbol{Q}$ is twofold [17], [19]: a) $\boldsymbol{Q}$ should be selected to leave the large singular values of $\boldsymbol{H}$ unchanged while moving the small singular values away from zero without introducing new small singular values in the inverse of (2.15). b) $\boldsymbol{Q}$ incorporates *a priori* knowledge in the restoration process about $\boldsymbol{f}$. In restoring images with random noise, smoothly varying images are usually desired, thus smoothness is the *a priori* knowledge on which the selection of $\boldsymbol{Q}$ is usually based upon.

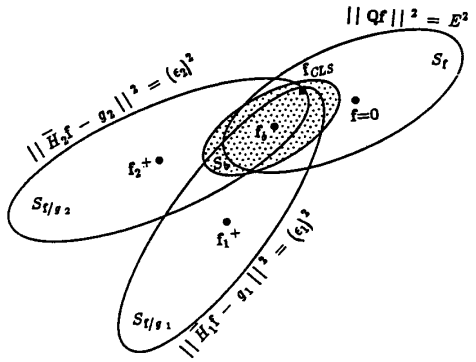

Fig. 1. The geometric interpretation using ellipsoids of the set theoretic f_b and the constrained optimization f_{CLS} solutions given by (2.10). The signal is a two-channel image.

A class of well-known regularization operators are the Tikhonov stabilizers [29], [30]. They are defined for a function $y(x)$ by

$$\|y\|_p = \sum_{r=0}^{p} \int_R B_r(x) \left(\frac{\partial^r y}{\partial x^r} \right)^2 dx \tag{2.18}$$

where $B_r(x)$ are nonnegative continuous weighting functions, R is the region of support, and $\partial^r y / \partial x^r$ denotes the rth partial derivative of y in terms of x.

For two-dimensional signals, the discrete version of a Tikhonov stabilizer with $p = 2$ and weights $B_0(x) = 0$, $B_1(x) = 0$, and $B_2(x) = 1$ is the discrete 2-D 3×3 Laplacian operator $\boldsymbol{Q}_{\text{2DL}}$. This operator has been used successfully in single-channel restoration problems [11]. It thus appears that regularization offers a theoretical basis for the smoothness constraint.

In a certain imaging situations, cross-channel smoothness is an important property of the multichannel images. Such examples are motion compensation of video frames and restoration of identical images observed through optical systems with different point-spread functions. In such cases, it is obvious that using a 3-D $3 \times 3 \times 3$ Laplacian $\boldsymbol{Q}_{\text{3DL}}$ visualized in Fig. 2 is advantageous over the two-dimensional Laplacian.

However, there exist applications that the channels exhibit strong cross-channel correlations but correlation varies from channel to channel. For those cases the 3-D Laplacian is not appropriate. Other regularization operators must be found that satisfy requirements a) and b) for the particular application of interest.

Color imagery is a special example of multichannel imagery. Different color planes contain registered versions of the same scene. Thus regions in the same spatial location appear to be similar across channels. However, because reflectivity properties depend on the light wavelength, these regions do not maintain the same magnitude across all color planes. Thus, it is expected that using the

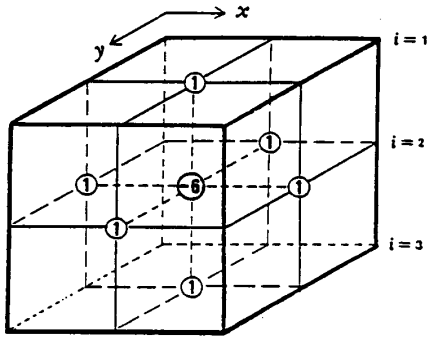

Fig. 2. The visualization of the three-dimensional Laplacian Q_{3DL} operator.

3-D 3 × 3 × 3 Laplacian of Fig. 2 will result in undesirable color smoothing. On the other hand, color planes are highly correlated and the 2-D Laplacian fails to capture between-channel similarities. It thus appears that for color images the selection between the 2-D and 3-D Laplacian is an issue of tradeoff between spatial detail and color smoothing.

However, we can get the best of both worlds by introducing a weighted 3-D operator Q_{3WL}. This operator is defined by a 3 × 3 × 3 convolutional mask q_{3WL}. Assuming that the center of the mask is at location (l, i, j) where l specifies the channel and i, j the spatial location, then

$$[Q_{3WL}f](l, i, j) = \sum_{k,m,n=-1}^{1} q_{3WL}(k, m, n) f(l - k, i - m, j - n) \tag{2.19}$$

where the weights of the mask are given by

$$q_{3WL}(1, 0, 0) = \frac{\|f_l\|}{\|f_{l+1}\|}, \qquad q_{3WL}(-1, 0, 0) = \frac{\|f_l\|}{\|f_{l-1}\|}$$

$$q_{3WL}(0, 0, -1) = q_{3WL}(0, 0, 1) = q_{3WL}(0, -1, 0) = q_{3WL}(0, 1, 0) = 1$$

$$q_{3WL}(0, 0, 0) = -6. \tag{2.20}$$

The cross-channel weights of this operator capture the changes of reflectivity across channels. Using this operator, color smoothing across channels can be avoided.

III. Computational Issues

The solution $\hat{f}$ in (2.15) requires the inversion of a $NM^2 \times NM^2$ matrix. For modest applications, for example, $M = 128$ and $N = 3$, the matrix inversion, if computed directly, requires the inversion of a 49 152 × 49 152 matrix.

In the case of single-channel images, the least squares estimate can be computed efficiently in the Fourier domain [11]. For multichannel images, the matrix

$$A = [H^t H + \Lambda^{-1} Q^t Q] \tag{3.1}$$

of (2.15) cannot be diagonalized via the DFT for the computation of the inverse. The degradation function H has submatrices H_{ij} which are $M^2 \times M^2$ block Toeplitz for linear spatially invariant imaging systems. However, $H_{ij} \neq H_{i+k,j+k}$, hence H is not a block-Toeplitz matrix.

The submatrices of Q, denoted as Q_{ij}, which describe the spatial properties of the image as well as the relationship across channels, are assumed to be block Toeplitz. However, Q itself is not block Toeplitz because $Q_{ij} \neq Q_{i+k,j+k}$. This can be explained by the fact that different channels embody different properties of the scene being imaged, and these differences can lead to substantial differences between the cross-channel property of the (i, j) image pair and that of the $(i + k, j + k)$ pair; therefore, there is no justification to assume that the pairwise cross-channel properties are invariant across all channels. In other words, different cross-channel constraints may be applied to different image pairs. Even in the special case when the same cross-channel constraints are applied to different channel pairs, that is, when $Q_{ij} = Q_{i+k,j+k}$, the term $\Lambda^{-1}Q^t$ in A is not block Toeplitz. This can be seen by examining

$$\Lambda^{-1}Q^t = \begin{bmatrix} \frac{1}{\lambda_1} Q^t_{11} & \frac{1}{\lambda_1} Q^t_{21} & \cdots & \frac{1}{\lambda_1} Q^t_{N1} \\ \frac{1}{\lambda_2} Q^t_{12} & \frac{1}{\lambda_2} Q^t_{22} & \cdots & \frac{1}{\lambda_2} Q^t_{N2} \\ \vdots & \vdots & \cdots & \vdots \\ \frac{1}{\lambda_N} Q^t_{1N} & \frac{1}{\lambda_N} Q^t_{2N} & \cdots & \frac{1}{\lambda_N} Q^t_{NN} \end{bmatrix} \tag{3.2}$$

since λ_i can be different for each submatrix.

The inverse term A in (3.1) is a block $NM^2 \times NM^2$ matrix containing submatrices A_{ij} which are products and sums of $M^2 \times M^2$ block Toeplitz matrices. The Toeplitz property is not maintained under multiplication; therefore, the submatrices A_{ij} are not Toeplitz and A itself is not Toeplitz.

However, using the block-Toeplitz to block-circulant approximation [10], submatrices H_{ij} and Q_{ij} become circulant. Furthermore, it is noted that the circulant property is maintained under multiplication; therefore A_{ij} are also block circulant, that is, although A is not block circulant, it is partitioned into block circulant submatrices.

This approximation has been theoretically justified. In [4] it was shown that the eigenstructure of non-Toeplitz block matrices that contain Toeplitz submatrices converges asymptotically as the size of the block increases (in our case M^2) to the eigenstructure of block matrices that contain the circulant approximations of the Toeplitz submatrices.

Based on the above observations and following identical steps as in [8], the computation of $\hat{f}$ in (2.15) can be implemented in the Fourier domain using block matrices with diagonal submatrices. The structure of those matri-

ces is given by

$$\begin{bmatrix} [\ ] & [\ ] & \cdots & [\ ] \\ [\ ] & [\ ] & \cdots & [\ ] \\ \vdots & \vdots & \cdots & \vdots \\ [\ ] & [\ ] & \cdots & [\ ] \end{bmatrix} \qquad \text{(Form D)}$$

where $[\ ]$ are $M^2 \times M^2$ diagonal submatrices. Operations on matrices of this form are computationally efficient because they contain only a few nonzero elements. Using the inversion procedure in [8] or the alternative method presented in Appendix C, $\hat{f}$ can be computed efficiently even when NM^2 is large.

IV. Spatially Adaptive Least Squares Restoration

In Section II-D it was noted that images with smooth transitions are in general desired by human viewers. This argument justifies the selection of the Tikhonov stabilizers as regularizing functionals for the formulation of the restoration problem. However, spatially localized physical transitions, such as abrupt changes in surface geometry, surface composition, surface reflectance characteristics, etc., give rise to discontinuities. Standard Tikhonov regularization with a constant regularizing coefficient over the entire image is not appropriate for these abrupt transitions [29].

In the least squares formulation of the restoration problem, this inherent limitation of standard Tikhonov stabilizers can be seen in the selection of the coefficients λ_i. The value of these coefficients is dependent on the average noise over the entire image. The values of λ_i express the desired tradeoff between fidelity to the observed data and smoothness of the solution. Using fixed values of λ_i over the entire image results in an averaging effect that blurs edges and enhances noise in smooth regions of the image.

For single-channel restoration a number of researchers have addressed this problem [13], [15]–[20]. A weighted norm formulation is used in [15], [16], [18], [20], in which the weights of the norm are based on the local properties of the image [13].

A similar approach could be used for the design of multichannel data-dependent least squares filters. Using the weighted norm approach of [31] (2.7) and (2.8) can be rewritten as

$$\|\boldsymbol{CQf}\|^2 \leq E^2 \qquad (4.1)$$

and

$$\|Z_i n_i\|^2 \leq \epsilon_i^2, \qquad i = 1, 2, \cdots, N \qquad (4.2)$$

where matrices Z_i and $\boldsymbol{C}$ are diagonal matrices of dimension $M^2 \times M^2$ and $NM^2 \times M^2N$, respectively. The diagonal elements of Z_i are equal to a measure of the spatial activity, while the diagonal elements of $\boldsymbol{C}$ are equal to the values of the visibility function [1], [13]. Using these weighted norms, the solution $\hat{f}$ is

$$\hat{f} = [\boldsymbol{H}^t\boldsymbol{Z}^t\boldsymbol{Z}\boldsymbol{H} + \Lambda\boldsymbol{Q}^t\boldsymbol{C}^t\boldsymbol{C}\boldsymbol{Q}]^{-1}\boldsymbol{H}^t\boldsymbol{Z}^t\boldsymbol{g} \qquad (4.3)$$

where $\boldsymbol{Z}$ is a $NM^2 \times M^2N$ block diagonal matrix with $M^2 \times M^2$ submatrices Z_i as diagonal elements. However, such a filter has a major drawback. It is impractical because of its computational cost. The diagonal matrices $\boldsymbol{Z}$ and $\boldsymbol{C}$ have different elements down the diagonal so they ruin the circulant structure of the submatrices in the inverse of (4.3).

To circumvent this problem, a measure of the local spatial activity was first applied to segment each image plane into a small number of regions of approximately equal spatial activity, as was done in [19] for single-channel images. Then, for each region, regularizing coefficients that match the spatial and cross-channel characteristics of that region are determined. This may be conceptualized as partitioning the image by a series of bandpass filters into regions based on their spatial frequency content. From the partitioned image it is possible to construct a set of restoration filters, each using a different λ_i and a different $\boldsymbol{Q}$.

The local spatial activity measure used was defined in [1] as

$$A(x, y) = \sum_{p=x-m}^{x+m} \sum_{q=y-n}^{y+n} B^{\|(x,y)-(p,q)\|} \cdot [|S_H(p, q)| + |S_V(p, q)|] \qquad (4.4)$$

where S_H and S_V are the horizontal and vertical slopes, $\|(x, y) - (p, q)\|$ is the Euclidean distance between locations (x, y) and (p, q), B is a constant controling the relative importance between the pixel at (x, y) and its neighbors, and (m, n) controls the size of the neighborhood around location (x, y). This measure $A(x, y)$ increases monotonically with the amount of the spatial activity in the two-dimensional neighborhood of the pixel at (x, y). The local variance has been used in [13] as a measure of the local spatial activity. In Section V we provide experimental results for this spatially adaptive approach.

V. Experiments

Experiments where performed to test the multichannel least squares filter.

To test the set theoretic formulation of Section II-A an estimate of the bound E^2 is required. Since $\boldsymbol{g}$ is usually a low-pass version of $\boldsymbol{f}$, and $\boldsymbol{Q}$ is a high-pass operator, for large SNR's $\|\boldsymbol{Qg}\|^2 \leq \|\boldsymbol{Qf}\|^2$. Thus the ellipsoid defined by $\|\boldsymbol{Qg}\|^2$ as the bound is contained in the ellipsoid defined by $\|\boldsymbol{Qf}\|^2$. In addition, the intersection of the ellipsoids S_{f/g_i} and $\|\boldsymbol{Qg}\|^2 = E^2$ is contained in the intersection of S_{f/g_i} and $\|\boldsymbol{Qf}\|^2 = E^2$. Thus the solution using $\|\boldsymbol{Qg}\|^2 = E^2$ satisfies all the constraints imposed by the available *a priori* information. In our experiments $\|\boldsymbol{Qg}\|^2$ was used as an estimate for E^2 in (2.7). It can be easily seen from the geometric interpretation of the set theoretic approach in Section II-A that this E-estimate yields smoother restoration results than using $\|\boldsymbol{Qf}\|^2$.

To test the constrained optimization approach the Lagrange multipliers were computed using Newton's method as described in Section II-B. The uniqueness of the solu-

tion was confirmed by using a number of different initial conditions.

In order to quantify the between-channel similarity of multichannel images a measure S_{ij} is used given by

$$S_{ij} = \left(\frac{f_i}{\|f_i\|}, \frac{f_j}{\|f_j\|} \right) \tag{5.1}$$

where $(,)$ is the inner product, $\| \ \|$ the L_2 norm, and i, j the channel indices. As pointed out in [24], this measure in contrast to the L_2 norm is insensitive to scaling.

Experiment One: This experiment was designed to test the two regularization operators, the 2-D Laplacian $\boldsymbol{Q}_{2DL}$ and the 3-D Laplacian $\boldsymbol{Q}_{3DL}$. Operator $\boldsymbol{Q}_{2DL}$ constrains $\hat{\boldsymbol{f}}$ to be spatially smooth within each channel, whereas $\boldsymbol{Q}_{3DL}$ constrains $\hat{\boldsymbol{f}}$ to have strong between-channel similarity, therefore a test image constructed by a set of identical images was used.

The green color plane of the Lena 128 × 128 image was used to construct a three-channel image. Known spatial degradation $\boldsymbol{H}$ was applied, where $\boldsymbol{H}$ is given by

$$\boldsymbol{H} = \begin{bmatrix} H_{11} & 0 & 0 \\ 0 & H_{22} & 0 \\ 0 & 0 & H_{33} \end{bmatrix} \tag{5.2}$$

and H_{ij} are $M^2 \times M^2$ block Toeplitz submatrices representing low-pass blurring filters implemented as convolution masks. Submatrix H_{11} represents a 5 × 5 uniform convolution operator with $1/25$ weights; H_{22} a 7 × 7 mask with $1/49$ weights; and H_{33} a 9 × 9 mask with $1/81$ weights. Finally, independent white Gaussian noise was added to each degraded image plane, resulting in 20, 30, and 40 dB SNR in channels 1, 2, and 3, respectively. The SNR was defined by

$$\text{SNR} = \frac{\|f_i\|^2}{\|n_i\|^2}. \tag{5.3}$$

Two filters based on $\boldsymbol{Q}_{2DL}$ and $\boldsymbol{Q}_{3DL}$ were applied. Since no cross-channel degradation is used in this experiment, $\boldsymbol{H}$ is block diagonal, therefore, the 2-D Laplacian operator is equivalent to restoring each channel separately by (2.19). The regularization coefficients $1/\lambda_i$ in this experiment were computed as Lagrange multipliers so $\hat{\boldsymbol{f}}$ satisfies the constraints of (2.11a). Mean-square error (MSE) was used to measure performance. The results of this experiment are tabulated in Table I. As expected, the 3-D Laplacian yielded superior results because it used cross-channel information to restore the identical image in all channels.

Experiment Two: This was designed to test both the set theoretic and the constrained optimization approach. Three regularization operators, $\boldsymbol{Q}_{2DL}$, $\boldsymbol{Q}_{3DL}$, and $\boldsymbol{Q}_{3WL}$ were used in each of the approaches. Operator $\boldsymbol{Q}_{3WL}$ constrains $\hat{\boldsymbol{f}}$ according to the cross-channel information estimated from the image, and real color images were used.

The three color components red, green, and blue of the 128 × 128 Lena image were blurred in the same way as in experiment one. The similarity measures defined by (5.1) for the three channels were computed and their values are tabulated in Table II. The values of the cross-channel weights for the $\boldsymbol{Q}_{3WL}$ operator were computed from both the original and the degraded image and are tabulated in Tables III and IV, respectively. Each of the three regularization operators was applied to both the set theoretic and constrained optimization filters. The results from this experiment are tabulated in Table V. From the results we see that $\boldsymbol{Q}_{3DL}$ yields better restoration than $\boldsymbol{Q}_{2DL}$. This can be explained by the fact that the three color components share some similarity which was verified by the measures in Table II. Thus, the 3-D in contrast to the 2-D Laplacian captured, even though not accurately, these cross-channel similarities. Operator $\boldsymbol{Q}_{3WL}$ yielded as expected even better MSE results than the two others. The resulting images are shown in Fig. 2.

From Table V we see that $1/\lambda_i$ when computed as Lagrange multipliers are larger than the ones computed by the set theoretic approach. This has been explained in Section II-D by the geometric interpretation of the two solutions. The constrained optimization method yields images that are smoother than the ones by the set theoretic approach, see Fig. 3 for the images. However, the set theoretic method requires less computation.

TABLE I
MULTICHANNEL LEAST SQUARES RESTORATION OF THREE IDENTICAL GREEN PLANES OF THE LENA 128 × 128 IMAGE. THE SNR IS 20, 30, AND 40 dB FOR CHANNELS 1, 2, AND 3, RESPECTIVELY. UNIFORM 5 × 5, 7 × 7, AND 9 × 9 BLURS WERE USED FOR THE RESPECTIVE CHANNELS. REGULARIZATION PARAMETERS $1/\lambda_i$ WERE COMPUTED AS LAGRANGE MULTIPLIERS

	Channel 1	Channel 2	Channel 3
Without restoration MSE	10.30	12.08	13.69
Using the two-dimensional Laplacian $\boldsymbol{Q}_{2DL}$			
$1/\lambda_i$	4.47E-02	3.83E-03	4.10E-04
Restoration MSE	8.21	7.70	
Using the three-dimensional Laplacian $\boldsymbol{Q}_{3DL}$			
$1/\lambda_i$	3.74E-02	2.53E-03	2.20E-04
Restoration MSE	6.48	6.35	6.10

TABLE II
SIMILARITY MEASURE S_{ij} GIVEN BY (3.24) FOR THE R, G, AND B COLOR PLANES OF THE LENA 128 × 128 IMAGE

$S_{RR} = 1.0$	$S_{RG} = 0.88$	$S_{RB} = 0.68$
$S_{GR} = 0.88$	$S_{GG} = 1.0$	$S_{RB} = 0.91$
$S_{BR} = 0.68$	$S_{BG} = 0.91$	$S_{BB} = 1.0$

TABLE III
THE RATIOS OF THE NORMS OF THE R, G, AND B COLOR PLANES OF THE ORIGINAL f LENA 128 × 128 IMAGE

$\frac{\|f_R\|}{\|f_R\|} = 1.0$	$\frac{\|f_R\|}{\|f_G\|} = 0.71$	$\frac{\|f_R\|}{\|f_B\|} = 1.12$
$\frac{\|f_G\|}{\|f_R\|} = 1.40$	$\frac{\|f_G\|}{\|f_G\|} = 1.0$	$\frac{\|f_G\|}{\|f_B\|} = 1.57$
$\frac{\|f_B\|}{\|f_R\|} = 0.88$	$\frac{\|f_B\|}{\|f_G\|} = 0.63$	$\frac{\|f_G\|}{\|f_B\|} = 1.0$

TABLE IV
THE RATIOS OF THE NORMS OF THE R, G, AND B COLOR PLANES OF THE DEGRADED g LENA 128 × 128 IMAGE

$\frac{\|f_R\|}{\|f_R\|} = 1.0$	$\frac{\|f_R\|}{\|f_G\|} = 0.78$	$\frac{\|f_R\|}{\|f_B\|} = 1.35$
$\frac{\|f_G\|}{\|f_R\|} = 1.26$	$\frac{\|f_G\|}{\|f_G\|} = 1.0$	$\frac{\|f_G\|}{\|f_B\|} = 1.71$
$\frac{\|f_B\|}{\|f_R\|} = 0.73$	$\frac{\|f_B\|}{\|f_G\|} = 0.58$	$\frac{\|f_G\|}{\|f_B\|} = 1.0$

TABLE V
MULTICHANNEL LEAST SQUARES RESTORATION OF THE COLOR LENA 128 × 128 IMAGE. UNIFORM 5 × 5, 7 × 7, AND 9 × 9 BLURS WERE USED FOR CHANNELS R, G, AND B, RESPECTIVELY. THE SNR IS 20, 30, AND 40 dB FOR THE RESPECTIVE CHANNELS

	Channel R	Channel G	Channel B
Without Restoration MSE	6.85	12.08	9.18
i) Using the Two-Dimensional Laplacian Q_{2DL}			
$1/\lambda_i$ Lagrange multipliers	5.08E-02	3.82E-03	3.42E-04
MSE after restoration	5.46	7.69	4.76
$1/\lambda_i$ Set theoretic	3.03E-03	5.96E-04	2.39E-05
MSE after restoration	5.65 (18%)	7.44 (38%)	4.90 (47%)
ii) Using the Three-Dimensional Laplacian Q_{3DL}			
$1/\lambda_i$ Lagrange multipliers	7.82E-03	1.45E-03	1.64E-04
MSE after restoration	4.34	6.61	4.39
$1/\lambda_i$ Set theoretic	1.18E-03	2.33E-04	9.34E-06
MSE after restoration	4.91	6.20	4.65
iii) Using Q_{3WL} weights computed from original f image.			
$1/\lambda_i$ Lagrange multipliers	8.27E-03	1.85E-03	1.52E-04
MSE after restoration	4.40	6.19	4.41
$1/\lambda_i$ Set theoretic	1.49E-03	2.92E-04	1.17E-05
MSE after restoration	4.72	5.88	4.47
iv) Using Q_{3WL} weights computed from degraded g image.			
$1/\lambda_i$ Lagrange multipliers	7.41E-03	2.09E-03	1.59E-04
MSE after restoration	4.38	6.20	4.47
$1/\lambda_i$ Set theoretic	1.47E-03	2.89E-04	1.16E-05
MSE after restoration	4.80 (30%)	5.87 (51%)	4.47 (51%)

The results of three regularation operators are: i) Q_{2DL} the two-dimensional Laplacian. ii) Q_{3DL} the three-dimensional Laplacian. iii) Q_{3WL} with cross-channel weights from Table III. iv) Q_{3WL} with cross-channel weights from Table IV.

Two more 128 × 128 color images, the Balloon image from Kodak, and the Skiers image from the Image Processing Laboratory of the University of Wisconsin-Madison were used to test the multichannel filters. The between-channel similarity measures for these images were computed and shown in Tables VI and VII, respectively. It has been noted that the Skiers image has the strongest between-channel similarity followed by the Lena and the Balloon images. Both images were degraded in the same way as the color Lena image in the previous experiments. The set theoretic approach was used with regularization oeprators Q_{2DL} and Q_{3WL}. Weights for the Q_{3WL} operator were computed for both images and are shown in Tables VIII and IX. The regularization coefficients $1/\lambda_i$ were computed using $\|Qg\|^2 = E^2$. The results of this experiment are tabulated in Table X. In all cases, the three-dimensional operator Q_{3WL} produced superior results.

In order to quantify the results in Table X and the analogous results in Table V, we computed the percent improvement of the restored image (%). This measure was defined as

$$(\%) = 100 \times \left(1 - \frac{\|\hat{f} - f\|^2}{\|g - f\|^2}\right) \tag{5.4}$$

where g, f, and $\hat{f}$ are the degraded, original, and restored images, respectively. From Tables V and VI we obtain the average (%) improvement of the Q_{3WL} over the Q_{2DL} for the Skiers, Lena, and Balloon images to be 12.67%, 9.67%, and 2.0%, respectively. This ordering corresponds also to the ordering based on the magnitudes of the cross-channel similarities as shown in Tables XI, XII and II. Thus, we experimentally verified that stronger cross-channel similarity produces better multichannel restoration.

(a)

(b)

(c)

Fig. 3. (a) Original color Lena image. Left: red, middle: green, and right: blue. (b) Distorted color Lena image. Left: red, middle: green, and right: blue. (c) Restored color Lena image using the constrained optimization approach, Q_{2DL}, and $1/\lambda_i$ computed as Lagrange multipliers. Left: red, middle: green, and right: blue. (*Continued on next page.*)

Experiment Three: This experiment was designed to show the reverse effect of the previous experiment that single-channel restoration is superior to multichannel restoration when the channels are not highly correlated. In this case three unrelated image planes were chosen to construct a three-channel image; the green color plane from the Lena, the same from the Balloon, and the Skiers image. They were degraded in the same way as in the previous experiments. The similarity measures across the channels of this multichannel set of images are tabulated in Table XI. They are restored by the set theoretic approach using Q_{2DL} and Q_{3WL}. The cross-channel weights

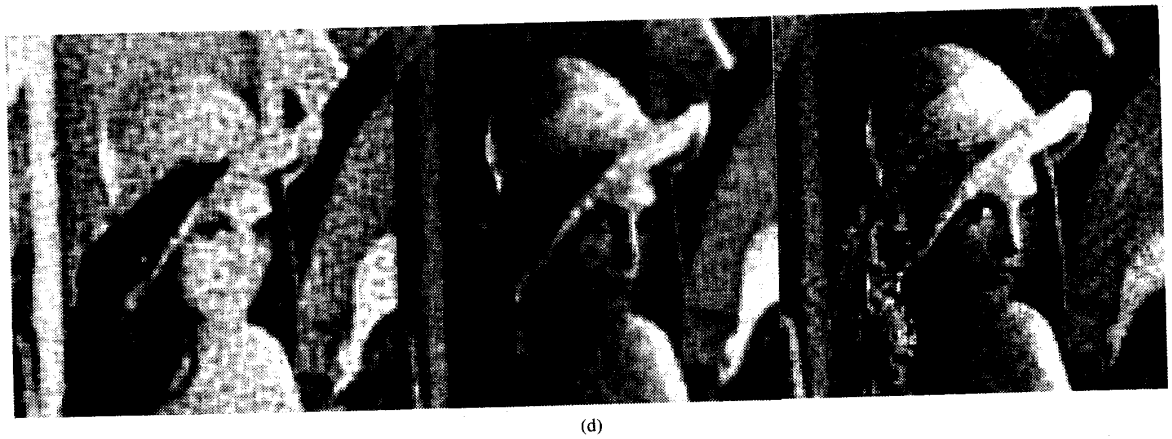

(d)

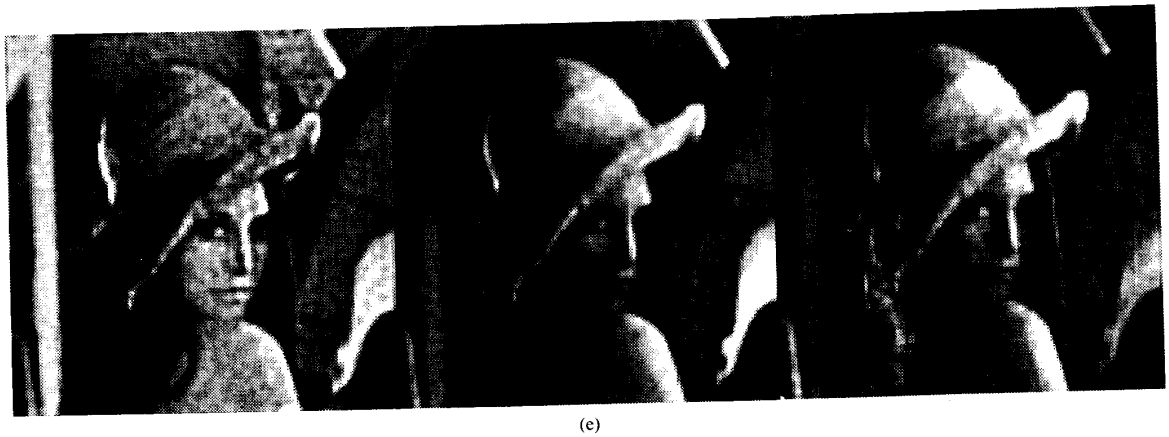

(e)

(f)

Fig. 3. (*Continued.*) (d) Restored color Lena image using the set theoretic approach, Q_{2DL}, and $1/\lambda_i$ computed by $\|Qg\|^2 = E^2$. Left, red, middle: green, and right: blue. (e) Restored color Lena image using the constrained optimization approach, Q_{3WL}, and $1/\lambda_i$ computed as Lagrange multipliers. Left: red, middle: green, and right: blue. (f) Restored color Lena image using the set theoretic approach, Q_{3WL}, and $1/\lambda_i$ computed by $\|Qg\|^2 = E^2$. Left: red, middle: green, and right: blue. (*Continued on next page.*)

of Q_{3WL} are tabulated in Table XII. The MSE results from this experiment are tabulated in Table XIII. Since the between-channel similarities are very weak, independent-channel is superior to multichannel restoration.

Experiment Four: The spatially adaptive filter described in Section V was tested. The color Lena image in experiment two was used. The image was segmented into five segments of approximately equal spatial activity. Based on visual examination, each segment was assigned a $1/\lambda_i$ value according to its smoothness. Note that $1/\lambda_i$

(g)

Fig. 3. (*Continued.*) (g) Restored color Lena image by the spatially adaptive filter using Q_{3AWL} and $1/\lambda_i$ based on Table XVI. Left: red, middle: green, and right: blue.

TABLE VI
THE SIMILARITY MEASURE S_{ij} GIVEN BY (6.1) FOR THE R, G, AND B COLOR PLANES OF THE SKIERS 128 × 128 IMAGE

$S_{RR} = 1.0$	$S_{RG} = 0.96$	$S_{RB} = 0.91$
$S_{GR} = 0.96$	$S_{GG} = 1.0$	$S_{RB} = 0.94$
$S_{BR} = 0.91$	$S_{BG} = 0.94$	$S_{BB} = 1.0$

TABLE VII
THE SIMILARITY MEASURE S_{ij} GIVEN BY (6.1) FOR THE R, G, AND B COLOR PLANES OF THE BALLOON 128 × 128 IMAGE

$S_{RR} = 1.0$	$S_{RG} = 0.76$	$S_{RB} = 0.57$
$S_{GR} = 0.76$	$S_{GG} = 1.0$	$S_{RB} = 0.64$
$S_{BR} = 0.57$	$S_{BG} = 0.64$	$S_{BB} = 1.0$

TABLE VIII
THE RATIOS OF THE NORMS OF THE R, G, AND B COLOR PLANES OF THE DEGRADED g SKIERS 128 × 128 IMAGE

$\frac{\|f_R\|}{\|f_R\|} = 1.0$	$\frac{\|f_R\|}{\|f_G\|} = 0.99$	$\frac{\|f_R\|}{\|f_B\|} = 1.04$
$\frac{\|f_G\|}{\|f_R\|} = 1.0$	$\frac{\|f_G\|}{\|f_G\|} = 1.0$	$\frac{\|f_G\|}{\|f_B\|} = 1.04$
$\frac{\|f_B\|}{\|f_R\|} = 0.96$	$\frac{\|f_B\|}{\|f_G\|} = 0.95$	$\frac{\|f_G\|}{\|f_B\|} = 1.0$

TABLE IX
THE RATIOS OF THE NORMS OF THE R, G, AND B COLOR PLANES OF THE DEGRADED g BALLOON 128 × 128 IMAGE

$\frac{\|f_R\|}{\|f_R\|} = 1.0$	$\frac{\|f_R\|}{\|f_G\|} = 1.17$	$\frac{\|f_R\|}{\|f_B\|} = 1.31$
$\frac{\|f_G\|}{\|f_R\|} = 0.85$	$\frac{\|f_G\|}{\|f_G\|} = 1.0$	$\frac{\|f_G\|}{\|f_B\|} = 1.11$
$\frac{\|f_B\|}{\|f_R\|} = 0.76$	$\frac{\|f_B\|}{\|f_G\|} = 0.89$	$\frac{\|f_G\|}{\|f_B\|} = 1.0$

in Table XIV are arranged in decreasing order corresponding to the segment's spatial activity. Four regularization operators were used; Q_{2DL}, Q_{3DL}, Q_{3WL}, and the

TABLE X
MULTICHANNEL LEAST SQUARES RESTORATION OF THE COLOR SKIERS, AND BALLOON, 128 × 128 IMAGES. THE SNR IS 20, 30, AND 40 dB FOR CHANNELS R, G, AND B, RESPECTIVELY. REGULARIZATION PARAMETERS $1/\lambda_i$ WERE COMPUTED USING $\|Qg\|^2 = E^2$. UNIFORM 5 × 5, 7 × 7, AND 9 × 9 BLURS WERE USED FOR CHANNELS R, G, AND B, RESPECTIVELY

	Channel R	Channel G	Channel B
Color Skiers 128 × 128 Image			
Before Restoration MSE	15.03	17.40	19.19
Using the Two-Dimensional Laplacian Q_{2DL}			
$1/\lambda_i$	3.78E-02	4.21E-03	4.20E-05
Restoration MSE	11.48 (24%)	10.63 (39%)	9.03 (53%)
Using the Three-Dimensional Weighted Q_{3WL} Operator.			
$1/\lambda_i$	2.34E-03	2.60E-04	2.60E-05
Restoration MSE	8.31 (45%)	8.18 (53%)	7.80 (59%)
Color Balloon 128 × 128 Image			
Before restoration MSE	14.91	13.91	14.77
Using the Two-Dimensional Laplacian Q_{2DL}			
$1/\lambda_i$	4.64E-03	3.53E-04	3.09E-05
Restoration MSE	12.30 (18%)	9.88 (29%)	8.74 (41%)
Using the Three-Dimensional Weighted Q_{3WL} Operator.			
$1/\lambda_i$	1.42E-03	1.08E-04	9.49E-06
Restoration MSE	11.52 (23%)	9.16 (34%)	8.79 (40%)

TABLE XI
THE SIMILARITY MEASURES S_{ij} GIVEN BY (5.1) FOR THE THREE CHANNELS, LENA-GREEN (CHANNEL 1), BALLOON-GREEN (CHANNEL 2), AND SKIERS-GREEN (CHANNEL 3)

$S_{11} = 1.0$	$S_{12} = 0.14$	$S_{13} = 0.19$
$S_{21} = 0.14$	$S_{22} = 1.0$	$S_{23} = 0.17$
$S_{31} = 0.19$	$S_{32} = 0.17$	$S_{33} = 1.0$

spatially adaptive three-dimensional operator Q_{3AWL}. The cross-channel weights of Q_{3AWL} were computed in the same way as those of Q_{3WL}. However, there were five separate sets of weights, one for each segment, for the Q_{3AWL} operator. This operator was used to capture the spatial changes of the reflectivity across channels. The MSE results of this experiment were tabulated in Table XV. The resulting images for Q_{3AWL} are shown in Fig. 3(g). Spatially adaptive least squares restoration is supe-

TABLE XII
THE RATIOS OF THE NORMS FOR THE THREE DEGRADED IMAGES LENA-GREEN (CHANNEL 1), BALLOON-GREEN (CHANNEL 2), AND SKIERS-GREEN (CHANNEL 3)

$\frac{\|f_1\|}{\|f_1\|} = 1.0$	$\frac{\|f_1\|}{\|f_2\|} = 0.72$	$\frac{\|f_1\|}{\|f_3\|} = 0.69$
$\frac{\|f_2\|}{\|f_1\|} = 1.38$	$\frac{\|f_2\|}{\|f_2\|} = 1.0$	$\frac{\|f_2\|}{\|f_3\|} = 0.96$
$\frac{\|f_3\|}{\|f_1\|} = 1.44$	$\frac{\|f_3\|}{\|f_2\|} = 1.04$	$\frac{\|f_2\|}{\|f_3\|} = 1.0$

TABLE XIII
MULTICHANNEL LEAST SQUARES RESTORATION OF THE THREE CHANNELS, LENA-GREEN (CHANNEL 1), BALLOON-GREEN (CHANNEL 2), AND SKIERS-GREEN (CHANNEL 3). THE SNR IS 20, 30 AND 40 dB FOR CHANNELS 1, 2, AND 3, RESPECTIVELY. UNIFORM 5×5, 7×7, AND 9×9 BLURS WERE USED FOR THE RESPECTIVE CHANNELS. REGULARIZATION PARAMETERS $1/\lambda_i$ WERE COMPUTED USING $\|\boldsymbol{Qg}\|^2 = E^2$

	Channel 1	Channel 2	Channel 3
Without restoration MSE	10.30	13.91	19.03
Using the Two-Dimensional Laplacian $\boldsymbol{Q}_{2DL}$			
$1/\lambda_i$	2.34E-03	4.30E-04	5.40E-05
Restoration MSE	8.72	6.90	8.71
Using the Three-Dimensional Weighted $\boldsymbol{Q}_{3WL}$ Operator			
$1/\lambda_i$	3.10E-04	5.96E-05	7.14E-06
Restoration MSE	11.26	11.93	11.35

TABLE XIV
THE VALUES OF $1/\lambda_i$ FOR THE SPATIALLY ADAPTIVE LEAST SQUARES FILTER

Segment Number	Channel R	Channel G	Channel B
1	1.0E-02	1.0E-03	1.0E-04
2	5.0E-03	5.0E-04	5.0E-05
3	1.0E-03	1.0E-04	1.0E-05
4	5.0E-04	5.0E-05	5.0E-06
5	1.0E-04	1.0E-05	1.0E-06

TABLE XV
MULTICHANNEL SPATIALLY ADAPTIVE LEAST SQUARES RESTORATION OF THE COLOR LENA 128×128 IMAGE. THE SNR IS 20, 30, AND 40 dB FOR CHANNELS R, G, AND B, RESPECTIVELY. UNIFORM 5×5, 7×7, AND 9×9 BLURS WERE USED FOR THE RESPECTIVE CHANNELS. THE VALUES FOR $1/\lambda_i$ ARE IN TABLE XIV

	Channel R	Channel G	Channel B
MSE Using $\boldsymbol{Q}_{2DL}$	5.27	7.16	4.26
MSE Using $\boldsymbol{Q}_{3DL}$	4.09	5.77	3.75
MSE Using $\boldsymbol{Q}_{3WL}$	4.08	5.55	3.73
MSE Using $\boldsymbol{Q}_{3AWL}$	4.05	5.46	3.72

rior to the others both visually and in terms of MSE (see Tables V and XI). It is noted that the improvement of the operator $\boldsymbol{Q}_{3AWL}$ over the operator $\boldsymbol{Q}_{3WL}$ was very small.

Experiment Five: In this experiment both within-channel and cross-channel blur were used. Channels 1–3 correspond to the red, green, and blue image planes, respectively. The color Lena image was degraded by a known degradation matrix $\boldsymbol{H}$ given by

$$\boldsymbol{H} = \begin{bmatrix} 0.5\,H_{11} & 0.3\,H_{12} & 0.2\,H_{13} \\ 0.25\,H_{21} & 0.5\,H_{22} & 0.25\,H_{23} \\ 0.2\,H_{31} & 0.3\,H_{32} & 0.5\,H_{33} \end{bmatrix} \tag{5.5}$$

and H_{ij} are $M^2 \times M^2$ block Toeplitz submatrices representing low-pass blurring filters implemented as convolution masks. Submatrices H_{11}, H_{12}, H_{13} represent a 5×5 uniform convolution operator with $1/25$ weights; H_{21}, H_{22}, H_{23} a 7×7 mask with $1/49$ weights; and H_{31}, H_{32}, H_{33} a 9×9 mask with $1/81$ weights. Finally, independent white Gaussian noise was added to each degraded image plane, resulting in 30-dB SNR in all channels.

TABLE XVI
MULTICHANNEL AND SINGLE-CHANNEL CONSTRAINED LEAST SQUARES RESTORATION OF THE COLOR LENA 128×128 IMAGE. THE IMAGE WAS BLURRED USING BOTH CROSS- AND WITHIN-CHANNEL BLUR. THE SNR IS 30 IN ALL CHANNELS

	Channel R	Channel G	Channel B
MSE Before restoration	8.31	13.64	10.80
Multichannel Restoration $H_{ij} \neq 0$ for $i \neq j$			
Using $\boldsymbol{Q}_{3WL}$ value of $1/\lambda_i$	6.41E-04	6.92E-04	5.01E-04
MSE using $\boldsymbol{Q}_{3WL}$	4.48	6.57	5.25
Using $\boldsymbol{Q}_{2DL}$ value of $1/\lambda_i$	9.93E-04	1.66E-03	1.09E-03
MSE using $\boldsymbol{Q}_{2DL}$	6.79	8.89	7.12
Single-Channel Restoration $H_{ij} = 0$ for $i \neq j$			
Using $\boldsymbol{Q}_{2DL}$ values of $1/\lambda_i$	3.64E-03	5.78E-03	2.65E-03
MSE using the $\boldsymbol{Q}_{2DL}$	6.98	9.23	7.93

In this experiment, the constrained optimization was used to derive the least squares filters. Both single and multichannel least squares filters were used. The single-channel filter was implemented using (2.17) with $\boldsymbol{Q}_{2DL}$ while ignoring the cross-channel degradations, that is, $H_{ij} = 0$ with $i \neq j$. The multichannel filters were implemented with $\boldsymbol{Q}_{2DL}$ and $\boldsymbol{Q}_{3WL}$ using the full $\boldsymbol{H}$ as given by (5.5). The MSE results of this experiment are tabulated in Table XVI. Using $\boldsymbol{Q}_{3WL}$ results in a drastic improvment over $\boldsymbol{Q}_{2DL}$, also, as expected, multichannel restoration is superior to single-channel restoration.

VI. CONCLUSIONS

In this paper least squares filters for multichannel images were developed. They offer an alternative to multichannel Wiener filtering [8] when accurate estimates of the multichannel statistics are not available. Two approaches, the set theoretic and the constrained optimization, were investigated. It has been demonstrated by a geometrical interpretation that the constrained optimization solution is smoother than the set theoretic one.

Color imagery was used as an example in multichannel restoration. Three regularizing operators that capture the between and within-channel properties of color images were used in the filter implementation. In addition, a spa-

tially adaptive algorithm was proposed to handle problems associated with local image spatial variations.

Experiments were performed and the following conclusions were reached.

a) For images with strong between-channel similarity, multichannel restoration always outperforms single-channel restoration.

b) The constrained optimization approach produces smoother images than the set theoretic approach, even with a rough estimate of E^2.

c) The spatially adaptive algorithm produces superior results in terms of MSE and visual quality.

Appendix A
Equation for the Center of the Bounding Ellipsoid

Clearly, the actual observation g_i specifies a set S_{f/g_i} which must contain f according to (2.5). More specifically, the set S_{f/g_i} because of (2.4) can be written as

$$S_{f/g_i} = [f : (\overline{H}_i f - g_i)^t (1/\epsilon_i)^2 (\overline{H}_i f - g_i) \leq 1] \quad \text{(A.1)}$$

$$= [f : (\overline{H}_i f - \overline{H}_i f_i^+)^t (1/\epsilon_i)^2 (\overline{H}_i f - \overline{H}_i f_i^+) \leq 1] \quad \text{(A.2)}$$

$$= [f : (f - f_i^+)^t (\overline{H}_i^t \overline{H}_i / \epsilon_i^2)(f - f_i^+)^t < 1]. \quad \text{(A.3)}$$

In obtaining (A.3) it was assumed that $g_i \in R(\overline{H}_i)$, where $R(\overline{H}_i)$ is the range of $\overline{H}_i$. Then, $f_i^+ = \overline{H}_i^+ g_i$, where $\overline{H}_i^+$ the generalized inverse of $\overline{H}_i$.

Consider now the general case of $N + 1$ ellipsoids

$$S_m = [f : (f - c_m)^t G_m^{-1} (f - c_m) \leq 1]$$
$$m = 1, 2, \cdots, N + 1. \quad \text{(A.4)}$$

The ellipsoid

$$S_b = [f : (f - c_b)^t G_b^{-1} (f - c_b) \leq 1] \quad \text{(A.5)}$$

which bounds the intersection of the $N + 1$ ellipsoids of (A.4) is characterized by [26]

$$c_b = \overline{G}_b \left(\sum_{m=1}^{N+1} p_m G_m^{-1} c_m \right) \quad \text{(A.6)}$$

and

$$\overline{G}_b^{-1} = \sum_{m=1}^{N+1} p_m G_m^{-1} \quad \text{(A.7)}$$

for $p_m > 0$ and $\Sigma_{m=1}^{N+1} p_m \leq 1$. Substituting

$$G_{N+1}^{-1} = \boldsymbol{Q}^t \boldsymbol{Q} / E^2, \qquad c_{N+1} = 0 \quad \text{(A.8)}$$

and

$$G_i^{-1} = \overline{H}_i^t \overline{H}_i / \epsilon_i^2, \qquad c_i = f_i^+ = (\overline{H}_i^t \overline{H}_i)^{-1} (\overline{H}_i g_i)$$
$$\text{for } i = 1, 2, \cdots, N \quad \text{(A.9)}$$

in (A.6), we get

$$c_b = \left[\sum_{i=1}^{N} p_i \frac{\overline{H}_i^t \overline{H}_i}{\epsilon_i^2} + p_{N+1} \frac{\boldsymbol{Q}^t \boldsymbol{Q}}{E^2} \right]^{-1} \cdot \left[\sum_{i=1}^{N} p_i \frac{(\overline{H}_i^t \overline{H}_i)(\overline{H}_i^t \overline{H}_i)^{-1} \overline{H}_i^t g_i}{\epsilon_i^2} + p_{N+1} \frac{\boldsymbol{Q}^t \boldsymbol{Q}}{E^2} 0 \right] \quad \text{(A.10)}$$

which yields (2.9).

Appendix B
Computing the Jacobian of $Z_i(\lambda_1, \lambda_2, \cdots, \lambda_N)$

The (i, j) element of the Jacobian of the function $Z_i(\lambda_1, \lambda_2, \cdots, \lambda_N)$ is given by

$$\frac{\partial Z_i(\lambda_1, \lambda_2, \cdots, \lambda_N)}{\partial (\lambda_j)^{-1}} = \boldsymbol{J}_{ij} = \frac{\partial \| \overline{H}_i \hat{f} - g_i \|^2}{\partial (\lambda_j)^{-1}}. \quad \text{(B.1)}$$

Let us write

$$\hat{f} = \boldsymbol{A}^{-1} \boldsymbol{H}^t \boldsymbol{g} \quad \text{(B.2)}$$

where

$$\boldsymbol{A} = [\boldsymbol{H}^t \boldsymbol{H} + \Lambda^{-1} \boldsymbol{Q}^t \boldsymbol{Q}]. \quad \text{(B.3)}$$

Using (B.2) and the property

$$\frac{\partial \boldsymbol{A}^{-1}}{\partial x} = -\boldsymbol{A}^{-1} \frac{\partial \boldsymbol{A}}{\partial x} \boldsymbol{A}^{-1} \quad \text{(B.4)}$$

the derivative of (B.1) can be written as

$$\frac{\partial \| \overline{H}_i \hat{f} - g_i \|^2}{\partial (\lambda_j)^{-1}} = -\boldsymbol{g}^t \boldsymbol{H} \boldsymbol{A}^{-t} \frac{\partial \boldsymbol{A}^t}{\partial (\lambda_j)^{-1}} \boldsymbol{A}^{-t} \overline{H}_i^t \overline{H}_i \boldsymbol{A}^{-1} \boldsymbol{H}^t \boldsymbol{g} - \boldsymbol{g}^t \boldsymbol{H} \boldsymbol{A}^{-t} \overline{H}_i^t \overline{H}_i \boldsymbol{A}^{-1} \frac{\partial \boldsymbol{A}}{\partial (\lambda_j)^{-1}} \boldsymbol{A}^{-1} \boldsymbol{H}^t \boldsymbol{g} + 2 g_i \overline{H}_i \boldsymbol{A}^{-1} \frac{\partial \boldsymbol{A}}{\partial (\lambda_j)^{-1}} \boldsymbol{A}^{-1} \boldsymbol{H}^t \boldsymbol{g}. \quad \text{(B.5)}$$

Equation (B.3) can be equivalently written as

$$\boldsymbol{A} = \left[\boldsymbol{H}^t \boldsymbol{H} + \sum_{k=1}^{N} (\lambda_k)^{-1} \boldsymbol{I}_{kk} \boldsymbol{Q}^t \boldsymbol{Q} \right] \quad \text{(B.6)}$$

with

$$\boldsymbol{I}_{kk} = \begin{bmatrix} [\boldsymbol{0}] & [\boldsymbol{0}] & \cdots & [\boldsymbol{0}] & \cdots & [\boldsymbol{0}] \\ [\boldsymbol{0}] & [\boldsymbol{0}] & \cdots & [\boldsymbol{0}] & \cdots & [\boldsymbol{0}] \\ \vdots & \vdots & \cdots & [\boldsymbol{I}] & \cdots & \vdots \\ [\boldsymbol{0}] & [\boldsymbol{0}] & \cdots & [\boldsymbol{0}] & \cdots & [\boldsymbol{0}] \end{bmatrix} \quad \text{(B.7)}$$

where $\boldsymbol{I}_{kk}$ is an $NM^2 \times M^2 N$ matrix, $[\boldsymbol{0}]$ represents an $M^2 \times M^2$ zero matrix and $[\boldsymbol{I}]$ an identity $M^2 \times M^2$ matrix at location (k, k). Using this notation we have

$$\frac{\partial \boldsymbol{A}}{\partial (\lambda_j)^{-1}} = \boldsymbol{I}_{jj} \boldsymbol{Q}^t \boldsymbol{Q}. \quad \text{(B.8)}$$

Finally, using (B.8), (B.5) yields the (i, j)th element of the Jacobian equal to

$$\boldsymbol{J}_{ij} = \frac{\partial \| \overline{\boldsymbol{H}}_i \hat{\boldsymbol{f}} - \boldsymbol{g}_i \|^2}{\partial (\lambda_j)^{-2}} = -2(\overline{\boldsymbol{H}}_i \hat{\boldsymbol{f}} - \boldsymbol{g}_i)^t \overline{\boldsymbol{H}}_i \boldsymbol{A}^{-1} \boldsymbol{I}_{jj} \boldsymbol{Q}^t \boldsymbol{Q} \hat{\boldsymbol{f}}. \tag{B.9}$$

Appendix C
Computing Inverses of Form D Matrices

Assume $\boldsymbol{D}$ is a $NM^2 \times M^2N$ form D matrix given by

$$\boldsymbol{D} = \begin{bmatrix} D(1,1) & D(2,1) & \cdots & D(N,1) \\ D(1,2) & D(2,2) & \cdots & D(N,2) \\ \vdots & \vdots & \cdots & \vdots \\ D(1,N) & D(2,N) & \cdots & D(N,N) \end{bmatrix} \tag{C.1}$$

with $D(i,j)\,M^2 \times M^2$ diagonal matrices and $i, j = 1, 2, \cdots, N$. We define by D^k, $k = 1, 2, \cdots, M^2$, the $N \times N$ matrix

$$D^k = \begin{bmatrix} D^k(1,1) & D^k(2,1) & \cdots & D^k(N,1) \\ D^k(1,2) & D^k(2,2) & \cdots & D^k(N,2) \\ \vdots & \vdots & \cdots & \vdots \\ D^k(1,N) & D^k(2,N) & \cdots & D^k(N,N) \end{bmatrix} \tag{C.2}$$

with $D^k(i,j)$ the (k, k) element of the matrix $D(i,j)$ of (C.1). For nonsingular D^k, let B^k be its inverse, that is,

$$B^k D^k = I. \tag{C.3}$$

Clearly, the computation of B^k is a very easy task since $N << M$. Let us define the following $NM^2 \times M^2N$ form D matrix

$$\boldsymbol{B} = \begin{bmatrix} B(1,1) & B(1,2) & \cdots & B(1,N) \\ B(2,1) & B(2,2) & \cdots & B(2,N) \\ \vdots & \vdots & \cdots & \vdots \\ B(N,1) & B(N,2) & \cdots & B(N,N) \end{bmatrix} \tag{C.4}$$

with each $B(i,j)$ an $M^2 \times M^2$ diagonal matrix such that $B^k(i,j)$, the (i,j)th element of the matrix B^k in (C.3) is the (k, k) element of the diagonal matrix $B(i,j)$ in (C.4). Then due to (C.3)

$$\boldsymbol{B}\boldsymbol{D} = \boldsymbol{I} \tag{C.5}$$

where $\boldsymbol{I}$ is the $NM^2 \times M^2N$ identity matrix. Thus the inversion of $NM^2 \times M^2N$ form D matrix can be decomposed into M^2 inversions of $N \times N$ matrices.

Acknowledgment

The authors would like to acknowledge the assistance of Dr. M. Karacotsios with the multidimensional Newton method.

References

[1] G. Anderson and A. Netravali, "Image restoration based on a subjective criterion," *IEEE Trans. Syst., Man, Cybern.*, vol. SMC-6, no. 12, pp. 845-853, Dec. 1976.

[2] H. C. Andrews and B. R. Hunt, *Digital Image Restoration.* Englewood Cliffs, NJ: Prentice-Hall, 1977.

[3] D. Angwin and H. Kaufman, "Effects of modeling domains on recursive color image restoration," in *Proc. Int. Conf. Acoust., Speech, Signal Processing* (Dallas, TX), Apr. 1987.

[4] R. K. Bahr and J. A. Bucklew, "Optimal sampling schemes for the Gaussian hypothesis testing problem," *IEEE Trans. Acoust., Speech, Signal Processing*, vol. 38, no. 10, pp. 1677-1686, Oct. 1990.

[5] N. P. Galatsanos, "Restoration of multichannel images," Ph.D. dissertation, Univ. Wisconsin-Madison, Aug. 1989.

[6] N. P. Galatsanos and R. T. Chin, "Digital restoration of multichannel images," in *Proc. IEEE Int. Conf. Acoust., Speech, Signal Processing* (Dallas, TX), Apr. 1987, pp. 1244-1247.

[7] N. P. Galatsanos and R. T. Chin, "Restoration of color images by multichannel Kalman filtering," *IEEE Trans. Signal Processing*, this issue, pp. 2237-2252.

[8] N. P. Galatsanos and R. T. Chin, "Digital restoration of multichannel images," *IEEE Trans. Acoust., Speech, Signal Processing*, vol. ASSP-37, no. 3, pp. 415-421, Mar. 1989.

[9] D. Ghiglia, "Space-invariant deblurring given N independently blurred images of a common object," *J. Opt. Soc. Amer. A*, vol. 1, no. 4, pp. 398-402, Apr. 1982.

[10] R. M. Gray, "On the asymptotic eigenvalue distribution of Toeplitz matrices," *IEEE Trans. Inform. Theory*, vol. IT-18, pp. 725-730, Nov. 1972.

[11] B. R. Hunt, "The application of constrained least squares estimation to image restoration by digital computer," *IEEE Trans. Comput.*, vol. C-22, pp. 805-812, Sept. 1973.

[12] B. R. Hunt and O. Kubler, "Karhunen-Loeve multispectral image restoration, Part I: Theory," *IEEE Trans. Acoust., Speech, Signal Processing*, vol. ASSP-32, no. 3, pp. 592-600, June 1984.

[13] A. K. Katsaggelos, J. Biemond, R. Mersereau, and R. Schafer, "Nonstationary iterative image restoration," in *Proc. Int. Conf. Acoust., Speech, Signal Processing* (Tampa, FL), 1985, pp. 696-699.

[14] A. K. Katsaggelos, J. Biemond, R. M. Mersereau, and W. W. Schafer, "A general formulation of constrained iterative restoration algorithms," in *Proc. Int. Conf. Acoust., Speech, Signal Processing* (Tampa, FL), 1985, pp. 700-703.

[15] A. K. Katsaggelos, "Multiple input adaptive iterative image restoration algorithms," in *Proc. Int. Conf. Acoust., Speech, Signal Processing* (Dallas, TX), 1987, pp. 1179-1182.

[16] A. K. Katsaggelos and J. K. Paik, "Iterative color image restoration algorithms," in *Proc. Int. Conf. Acoust., Speech, Signal Processing* (New York, NY), 1988, pp. 1028-1032.

[17] A. K. Katsaggelos, "Iterative image restoration algorithms," *Opt. Eng.*, vol. 28, no. 7, pp. 735-748, July 1989.

[18] A. K. Katsaggelos, "A multiple input image restoration algorithm," *J. Visual Commun. Image Processing*, pp. 93-103, Sept. 1990.

[19] A. K. Katsaggelos, J. Biemond, R. W. Schafer, and R. M. Mersereau, "A regularized iterative image restoration algorithm," *IEEE Trans. Signal Processing*, vol. 39, no. 4, pp. 914-929, Apr. 1991.

[20] R. L. Lagendijk, J. Biemond, and D. E. Boekee, "Regularized iterative image restoration with ringing reduction," *IEEE Trans. Acoust., Speech, Signal Processing*, vol. ASSP-26, pp. 1874-1888, Dec. 1988.

[21] P. Meer, J. Jolion, and A. Rosenfeld, "A fast parallel algorithm for blind estimation of noise variance," *IEEE Trans. Pattern Analysis Mach. Intel.*, vol. PAMI-12, no. 2, pp. 216-222, Feb. 1990.

[22] K. Miller, "Least-squares method for ill-posed problems with a prescribed bound," *SIAM J. Math. Anal.*, vol. 1, pp. 52-74, Feb. 1970.

[23] N. Ohyama, M. Yachida, E. Badique, J. Tsujiuchi, and T. Honda, "Least squares filter for color-image restoration," *J. Opt. Soc. Amer. A*, vol. 5, no. 1, pp. 19-24, Jan. 1988.

[24] H. Peng and H. Stark, "Signal recovery with similarity constraints," *J. Opt. Soc. Amer. A*, vol. 6, no. 6, June 1989.

[25] J. L. C. Sanz and T. S. Huang, "Unified Hilbert space approach to iterative least square linear signal restoration," *J. Opt. Soc. Amer. A*, vol. 73, pp. 1455-1465, 1983.

[26] F. C. Schweppe, *Uncertain Dynamic Systems.* Englewood Cliffs, NJ: Prentice-Hall, 1973.

[27] M. Sezan and H. Trussel, "Use of *a priori* knowledge in multispectral image restoration," in *Proc. Int. Conf. Acoust., Speech, Signal Processing* (Glasgow, Scotland), 1989, pp. 1429-1432.

[28] A. M. Tekalp, H. Kaufman, and D. Angwin, "Adaptive restoration of color images," presented at the Yale Workshop Appl. Adaptive Syst. Theory, New Haven, CT, May 1987.

[29] D. Terzopoulos, "Regularization of inverse visual problems involv-

ing discontinuities," *IEEE Trans. Pattern Analysis Mach. Intel.*, vol. PAMI-8, no. 4, pp. 413–424, July 1986.
[30] A. Tikhonov and V. Arsenin, *The Solution to Ill-Posed Problems.* New York: Wiley, 1977.
[31] D. M. Titterington, "General structure of regularization procedures in image reconstruction," *Astron. Astrophys.*, vol. 144, pp. 381–387, 1985.
[32] H. J. Trussell, "Convergence criteria for iterative restoration methods," *IEEE Trans. Acoust., Speech, Signal Processing*, vol. ASSP-31, pp. 129–136, Feb. 1983.
[33] H. J. Trussell, "*A priori* knowledge in algebraic reconstruction methods," in *Advances in Computer Vision and Image Processing*, vol. I, *Image Reconstruction from Incomplete Observations*, T. S. Huang, Ed. JAI Press, 1984, pp. 265–316.

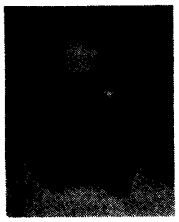

Nikolas P. Galatsanos (S'84–M'85) was born in Athens, Greece, in 1958. He received the Diploma degree in electrical engineering from the National Technical University of Athens, Athens, Greece, in 1982, the M.S. and the Ph.D. degrees, both in electrical engineering, from the University of Wisconsin-Madison, in 1984 and 1989, respectively.

Since August of 1989, he has been on the faculty of the Department of Electrical and Computer Engineering, Illinois Institute of Technology, Chicago, IL, where he is currently Assistant Professor. His current research interests include image restoration/reconstruction, image coding, and VLSI architectures for signal processing algorithms.

Dr. Galatsanos is a member of SPIE, OSA, and the Technical Chamber of Greece.

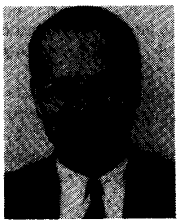

Aggelos K. Katsaggelos (S'80–M'85) was born in Arnea, Greece, on April 17, 1956. He received the Diploma degree in electrical and mechanical engineering from the Aristotelian University of Thessaloniki, Thessaloniki, Greece, in 1979, and the M.S. and Ph.D. degrees, both in electrical engineering, from the Georgia Institute of Technology, Atlanta, in 1981 and 1985, respectively.

From 1980 to 1985 he was a Research Assistant at the Digital Signal Processing Laboratory of the Electrical Engineering School, Georgia Institute of Technology. He is currently an Assistant Professor in the Department of Electrical Engineering and Computer Science at Northwestern University, Evanston, IL. During the 1986–1987 academic year he was an Assistant Professor at the Department of Electrical Engineering and Computer Science, Polytechnic University, Brooklyn, NY. He is also a member of the Associate Staff, Department of Medicine, Evanston Hospital. His current research interests include signal and image processing, processing of moving images, computational vision, and VLSI implementation of signal processing algorithms.

Dr. Katsaggelos is an Ameritech Fellow and a member of the SPIE, the Steering Committee of the IEEE TRANSACTIONS ON MEDICAL IMAGING, the IEEE-CAS Technical Committee on Visual Signal Processing and Communications, the Technical Chamber of Commerce of Greece, and Sigma Xi. He is an Associate Editor for the IEEE TRANSACTIONS ON SIGNAL PROCESSING and also Editor of the book *Digital Image Restoration* (Springer-Verlag, 1991).

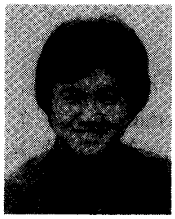

Roland T. Chin (S'75–M'79) received the B.S. degree with honors in 1975 and the Ph.D. degree in 1979 in electrical engineering from the University of Missouri, Columbia.

From 1979 to 1981, he was with Business and Technological Systems, Inc., Maryland, where he engaged in research in remote sensing data analysis and classification for NASA Godard Space Flight Center, Greenbelt, MD. Since 1981, he has been on the faculty of the Department of Electrical and Computer Engineering at the University of Wisconsin-Madison, where he is currently a Professor. His current research interests include image restoration, texture analysis, shape descriptions, pattern recognition, visual inspection, object recognition, and related applications.

Dr. Chin is a member of Eta Kappa Nu and Tau Beta Pi and he was the recipient of the 1984 Presidential Young Investigator Award.

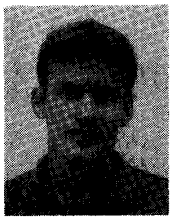

Allen D. Hillery (S'84–M'91) was born in Lancaster, WI, in 1962. He received the B.S. and Ph.D. degrees in electrical and computer engineering from the University of Wisconsin-Madison, in 1984 (honors) and 1991, respectively.

He is now with Shell Oil Research in Houston, TX. His research interests include image processing, digital signal processing, adaptive filtering, estimation and detection, and related applications.